nature materials

Article

https://doi.org/10.1038/s41563-026-02609-3

A $Sc_2C_2@C_{88}$-cluster-based ultra-compact multilevel probabilistic bit for matrix multiplication

Received: 5 August 2025

Accepted: 14 April 2026

Published online: 13 May 2026

Check for updates

Haoran Qi[1,2,3,9], Guohao Xi[4,9], Yuan-Biao Zhou[5,9], Xinrong Liu[1,2,3,9], Yifu Mao[1,2,3,9], Jian Yang[1,2,3], Jun Chen[1,2,3], Kuojuei Hu[1,2,3], Weiwei Gao[2,3], Shuai Zhang[1,2,3], Xiaoqin Gao[1], Jianguo Wan[1], Da-Wei Zhou[6], Junhong An[7], Xuefeng Wang[8], De-Chuan Zhan[6], Minhao Zhang[1,2,3] ✉, Cong Wang[4] ✉, Wei ji[4], Yuan-Zhi Tan[5] ✉, Su-Yuan Xie[5] & Fengqi Song[1,2,3] ✉

Information units are progressively approaching the fundamental physical limits of integration density, including in terms of extremely small sizes, multistates and probabilistic traversal. However, simultaneously encompassing all of these characteristics in a unit remains elusive. Here, via real-time in situ electrical monitoring, we clearly observed stochastic alterations of multiple conductance states in $Sc_2C_2@C_{88}$. The true random bit sequence generated exhibited an autocorrelation function whose confidence interval fell within ±0.02, demonstrating high-quality randomness. The alterations of multiple conductance states are controllable, that is, whose probability distributions could traverse from 0 to 1, enabling us to factorize 551 into its prime factors. Furthermore, we proposed a matrix-chain multiplication scheme and experimentally verified the multiplication of two 4 × 4 state-transition matrices with a small maximum error of <0.05. Combined with theoretical calculations, the stochastic but controllable multistates are probably attributed to the rich energy landscape, which could be stepwise changed by the electric field. Our findings reveal extremely small multilevel probabilistic bit for matrix multiplication, which pave the way for ultra-compact intelligent electronic devices.

Owing to the proliferation of big-data storage, machine learning and scientific computing applications, advanced information units are currently in greater demand than ever before[1,2]. First, there is an increasing demand for extremely small information units, such as storage or computing based on DNA[3–6], single atoms[7–11] and single molecules[12–17], as they allow a substantially increased data capacity within the same physical space. In addition, a multistate capability represents another critical requirement for advanced information units, as it enables a notable increase in data density by allowing the storage of more than one bit of information per cell[18–22].

Furthermore, probabilistic traversal within a single information unit, designated as a probabilistic bit (p-bit), has generated considerable interest in the development of alternative computing paradigms that address uncertainty issues and combinatorial optimization challenges[23,24]. For example, in prime factorization based on magnetic tunnel junctions (tens of nanometres), a low energy barrier enables the stochastic switching of magnetization between two states, assisted by thermal fluctuations[23]. Other nanosystems, such as magnetic skyrmions and manganite nanowires, also have the potential to implement the p-bit functionality[25,26].

However, demonstrating a unit that possesses all of these characteristics, that is, an extremely small size, a multistate capability and probabilistic traversal, is extremely difficult. Previous studies have

A full list of affiliations appears at the end of the paper. ✉e-mail: zhangminhao@nju.edu.cn; wcphys@ruc.edu.cn; yuanzhi_tan@xmu.edu.cn; songfengqi@nju.edu.cn

https://doi.org/10.1038/s41563-026-02609-3

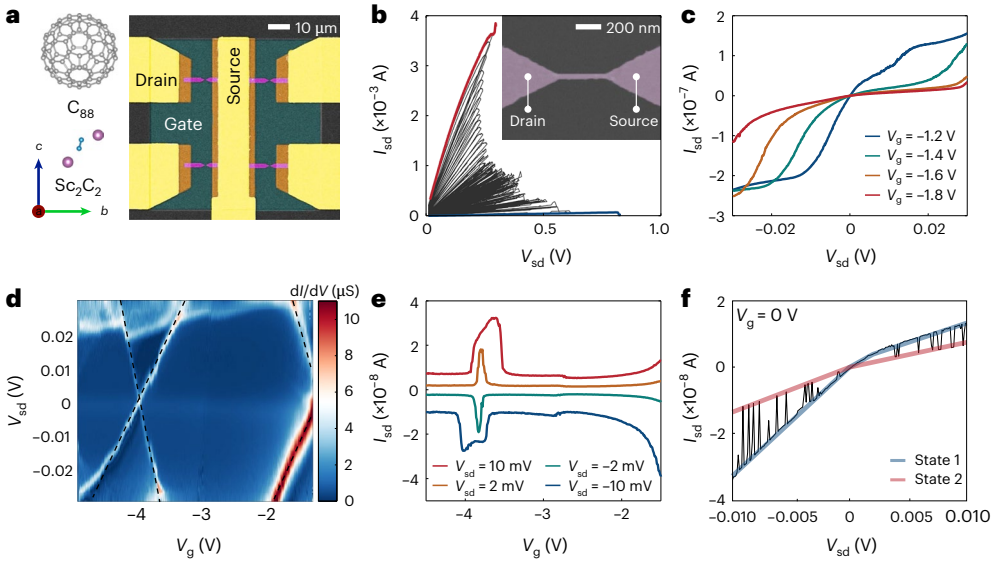

Fig. 1 | Single-electron transport of Sc_2C_2@C_{88} cluster. a, Schematic and electron micrograph of the Sc_2C_2@C_{88} device. **b**, Source–drain current (I_{sd})–voltage (V_{sd}) relationship during the FCEBJ process. The red line is the starting line, whereas the blue line is the ending line. The illustration shows a scanning electron microscopy image of the hourglass-shaped nanowire before the FCEBJ process. **c**, Coulomb blockade phenomenon at various V_g values in a Sc_2C_2@C_{88} transistor (device 1). **d**, Mapping of the differential conductance (dI/dV) as a function of V_{sd} and V_g. **e**, Current–gate voltage relationship extracted from the current mapping corresponding to the data in **d**. **f**, I_{sd}–V_{sd} curve at V_g = 0 V. According to the red and blue markings, device 1 exhibits a random switching behaviour.

demonstrated stochastic alterations in the conductance as seen by the scanning tunnelling microscopy technique at the atomic level[27–29], but translating these observations into scalable, batch-fabricated devices has been challenging. Recent studies on the single-cluster devices of endohedral fullerenes indicate electrically switchable electret/magnetism, carbon cage protection and possible multi-stable states[16,17,30], which shed light on a practical ultra-compact multilevel p-bit.

Here we report the electrically switchable stochastic alterations in conductance in a single Sc_2C_2@C_{88} cluster device. We investigate the statistical distributions and transition probability matrices of multiple conductance states. On the basis of the ultra-compact information unit, we showcase the probabilistic traversal capability in the prime factorization of 551 and the high-precision multiplication of two 4 × 4 matrices. Together with the theoretical calculations, we reveal that the rich energy landscape stepwise evolves with the electric field, which is likely to induce stochastic multistates and matrices.

Single-electron transport of Sc_2C_2@C_{88} cluster

Here we selected Sc_2C_2@C_s(hept)-C_{88} (<1 nm) as an ultra-compact unit (Fig. 1a) because the symmetry of the C_{88} cage, the orientation of the Sc_2C_2 molecule and the alignment of the C_2 dimer collectively endow it with a rich energy landscape. Here the energy landscape describes the relationship between the potential energy surface (PES) of the Sc_2C_2@C_{88} cluster and its internal configuration of the encapsulated Sc_2C_2 unit. Our devices feature a transistor architecture comprising source, drain and gate electrodes, as shown in the SEM image in Fig. 1a. At its core lies an hourglass-shaped nanowire (~50 nm at its narrowest) fabricated via electron-beam lithography, which is highlighted in Fig. 1a (pink) and magnified in Fig. 1b (inset). We then need to create a nanogap within this nanowire to establish a tunnelling contact between a Sc_2C_2@C_{88} cluster and the gold electrodes. Here we used the feedback-controlled electromigration break junction (FCEBJ) method at 1.8 K (refs. 16,30). The source–drain current (I_{sd})–voltage (V_{sd}) relationship during the FCEBJ process is shown in Fig. 1b. The red line is the starting line, whereas the blue line is the ending line. The Sc_2C_2@C_{88} solution was coated onto the devices in a glovebox before we conducted the FCEBJ procedure. More details regarding the device fabrication are provided in Supplementary Note 1.

After the FCEBJ process, we conducted I_{sd}–V_{sd} measurements to identify whether the Sc_2C_2@C_{88} transistors were successfully prepared. Unless otherwise noted, the current–voltage characteristics of devices shown were measured at a cryostat temperature of 2 K. For the successfully prepared Sc_2C_2@C_{88} transistors, the I_{sd}–V_{sd} curve usually reveals a nonlinear property with a distinct Coulomb blockade in the low-voltage region (Fig. 1c). The region could be further manipulated by the gate voltage, indicating that the electric field effectively manipulates the electrochemical potential of Sc_2C_2@C_{88}. Figure 1d shows the mapping of the differential conductance (dI/dV) as a function of the bias voltage (V_{sd}) and gate voltage (V_g) in a Sc_2C_2@C_{88} transistor (defined as device 1). The blue regions represent the Coulomb blockade regime, whereas the white and red regions indicate differential conductance peaks. For clarity, the Coulomb edges are marked with black dashed lines. On the basis of the Coulomb diamond pattern shown in Fig. 1d, the maximum charging energy of the device could be estimated (exceeding 75 meV), which indicated that the transport signal originates from Sc_2C_2@C_{88} rather than from a gold nanoparticle formed due to electromigration. Figure 1e shows the current–gate voltage relationship extracted from the current mapping corresponding to the data in Fig. 1d. Remarkably, the source–drain current randomly switches among at least two distinct current levels at V_g = 0 V, which are marked with red and blue lines (Fig. 1f). In this study, the probability of obtaining measurable tunnelling currents after the FCEBJ process was approximately 60%. Following FCEBJ, a total of 381 devices exhibited measurable tunnelling currents. Among these, Coulomb blockade features were observed in approximately 280 devices, and a stochastic switching behaviour was demonstrated in 73 devices. Examples of the fabricated stochastic switching elements are presented in Supplementary Note 2 and Supplementary Fig. 13.

Stochastic alterations of multiple conductance states

Among all the devices that exhibited a stochastic behaviour, we take device 2 as an example to investigate the detailed stochastic alterations

https://doi.org/10.1038/s41563-026-02609-3

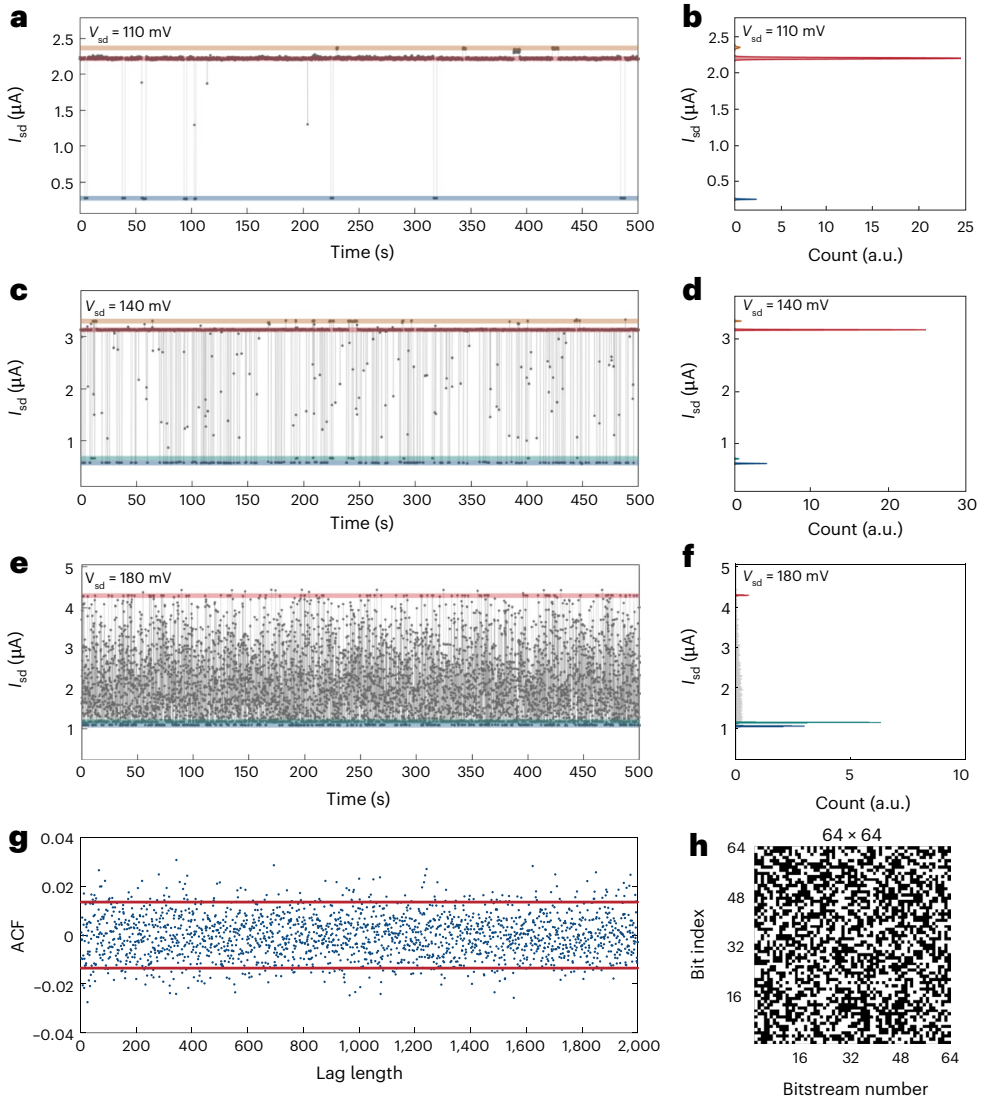

Fig. 2 | Stochastic alterations of multiple conductance states. a,**c**,**e**, Random switching between different conductance states at V_{sd} values of 110 mV (**a**), 140 mV (**c**) and 180 mV (**e**) (device 2), as shown in the *I*–*t* response. The total recording time for each dataset is 500 s. **b**,**d**,**f**, Current distributions at the corresponding voltages revealing three (**b**), four (**d**) and three (**f**) discrete states. **g**, Autocorrelation functions generated from two sets of *I*–*t* data using device 2 at a bias voltage of 140 mV. The ACF is less than 0.02 (95% confidence interval). **h**, A 64 × 64 code map plotted using the data from **g**.

of multiple conductance states. The current–time (*I*–*t*) measurements at V_{sd} = 110 mV exhibit random switching between three conductance states, as evidenced by the distinct current levels (Fig. 2a). A statistical histogram of the current distribution is plotted in Fig. 2b, revealing three discrete states marked in orange, red and blue. As shown in Fig. 2c,e, we measured the *I*–*t* response at different bias voltages, and the current distributions are plotted in Fig. 2d,f. The number of states and their distribution markedly change with the bias voltage: the device exhibits four discrete states at 140 mV and only three discrete states at 180 mV.

We also investigated the randomness of state transitions. We selected two sets of *I*–*t* responses at 140 mV and generated a 0–1 random number sequence. The confidence interval for the autocorrelation coefficient (ACF) of the sequence lies within ±0.02 (Fig. 2g). The ACF could be further decreased by increasing the measurement time (Supplementary Fig. 14). Compared with existing works[31–35], our autocorrelation results exhibit high-quality randomness. We also plot the 0–1 random number sequence in code maps (Fig. 2h), confirming the high-quality true random sequence generated.

Controllable alterations of multiple conductance states

Then, we measured the multiple conductance states at more bias voltages in device 2 and obtained the statistical distribution of the multi-states (Fig. 3a–f). As the voltage increases, the proportion of the two upper conductance states gradually decreases, whereas that of the lower conductance states gradually increases. We marked a comparative broken line based on the current distribution of the device (Fig. 3g, yellow line). The areas above and below the broken line are marked as 1 and 0, respectively. We plotted the probability distribution of the 0–1 states versus the bias voltage and fitted it with a sigmoid function (Fig. 3h), indicating that the probability can be controlled between 0 and 1. The p-bit function was also observed in other Sc_2C_2@C_{88} devices (Supplementary Note 4). Although stochastic conductance-state alterations have previously been observed in fullerenes[27,28], probabilistic traversal has not been achieved.

Controllable alterations of multiple conductance states enable us to realize probabilistic computing, like the integer factorization problem. The goal of the algorithm is to find the p-bit configuration

https://doi.org/10.1038/s41563-026-02609-3

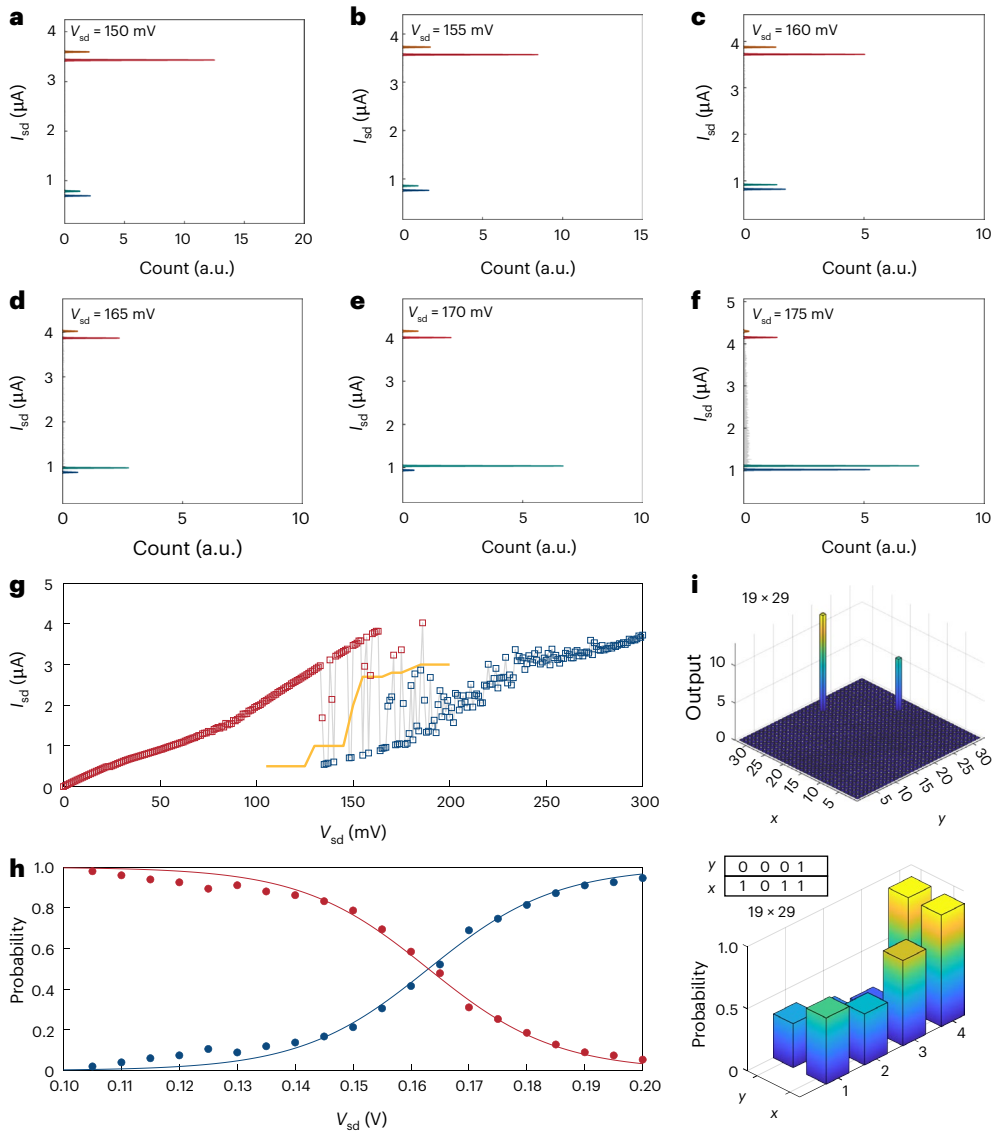

Fig. 3 | Controllable alterations of multiple conductance states. **a**–**f**, Regulation of voltage on the cluster conductance states, showcasing six different voltages (device 2). As the voltage increases gradually, the probability of the high-conductance states decreases, whereas the probability of the low-conductance states increases. **g**, Current–voltage response of the device and the division of conductance states. The yellow dashed line divides the device into two regions, namely, high and low, corresponding to 0 and 1, respectively. **h**, Voltage control of probability, demonstrating the gradual transition of device probability with voltage variation. **i**, Integer factorization results. For each integer to be factored, we performed 20 repeated calculations, all of which converged to the correct results. The factorization of 551 using 8-bit positions is shown. The data plot below shows the average probability distributions of the device at the termination of each factorization.

that minimizes E (see the 'Factorization algorithm' section). Specifically, we saved the voltage to be input in the form of an array, applied it sequentially to the p-bit unit and recorded the output of the p-bit unit in an array one by one (Supplementary Note 4). In this way, it equivalently reproduces the effect of multiple p-bits operating in parallel. The $Sc_2C_2@C_{88}$ device serves as the genuine, physical random number generator (p-bit). Specifically, a Keithley 2450 source meter simultaneously functions as a precision voltage source (digital-to-analogue converter) and a current meter (analogue-to-digital converter), applying the input bias to the device and directly reading its stochastic conductance state. A custom LabVIEW (NI LabVIEW 2023 Q3) program processes the real-time, probabilistic output stream from the $Sc_2C_2@C_{88}$ device, calculates the next input voltage based on the cost function and immediately commands the source meter to apply it. This creates a closed-loop, adaptive physical process in which each iteration of the algorithm depends on the instantaneous, unpredictable state of the $Sc_2C_2@C_{88}$ device. Figure 3i demonstrates the integer factorization results. For each integer to be factored, we repeated the calculation 20 times, and each calculation converged to the correct result: for 551, we found two peaks at (19, 29) and (29, 19). Figure 3i (bottom) displays the averaged probability distribution of the p-bit at each factorization termination. For example, for the target vector '1, 0, 1, 1' (decimal 29 = 1 × 2 + 0 × 4 + 1 × 8 + 1 × 16 + 3), the corresponding probabilities are 0.53, 0.41, 0.68 and 0.89. Positions at which the target is 1 are driven towards higher probabilities, whereas positions at which the target is 0 are driven towards lower probabilities, confirming the effectiveness of algorithmic control over the device.

High-precision matrix multiplication

In addition, we measured the probabilities of the device switching between different states within a specific time interval. As the probability distribution of the state in the next time interval depends

https://doi.org/10.1038/s41563-026-02609-3

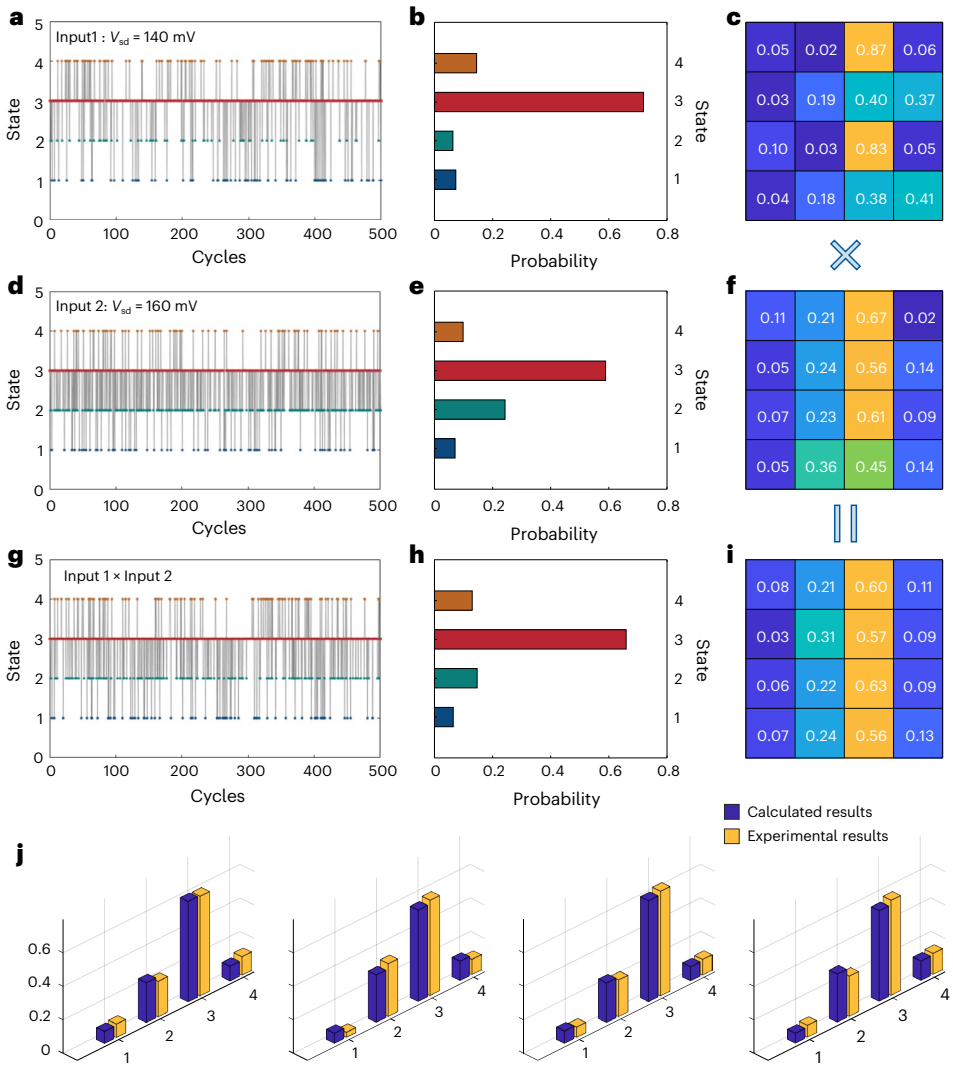

Fig. 4 | High-precision matrix multiplication. a, State–cycle response curves of device 2 under V_{sd} = 140 mV. The state of the device at the beginning and end of each cycle was recorded with a period of 1 s and plotted in the curve. Four different conductance states are indicated (a total of 1,500 cycles were recorded (Supplementary Note 7), and only representative sections are shown in the figures). **b**, State distribution histograms derived from the state–cycle responses in **a**. **c**, State transition matrices derived from the data in **a** (time interval of 1 s, matrix elements rounded to two decimal places). **d**, State–cycle response curves of device 2 under V_{sd} = 160 mV. **e**, State distribution histograms derived from the state–cycle responses in **d**. **f**, State-transition matrices derived from the data in **d**. **g**, State–cycle response curves of the device obtained by switching V_{sd} between 140 mV and 160 mV. Under a voltage of 140 mV, the initial state of the device is recorded. After a dwell time of 1 s, the voltage is switched to 160 mV, where it remains for another second before the final state of the device is recorded, completing one cycle. **h**, State distribution statistics corresponding to the data in **g**. **i**, State-transition matrix corresponding to the data in **g**. **j**, Comparison of the measured and calculated values of matrix multiplication: yellow data represent the measured values, and blue data represent the values obtained through direct calculation, with the maximum and average errors less than 0.05 and 0.03, respectively.

solely on its state in the present time interval (see the 'Discussion' section) and remains constant over time (Supplementary Note 5 and Supplementary Fig. 18), the sequence of state transitions forms a continuous-time Markov chain[36–40]. Through the Markov chain model, we represented the state transitions of the device in the form of a state-transition matrix. Exploiting the Markov chain's intrinsic properties, we designed tailor-made physical processes that can be tracked in real time, enabling high-precision matrix multiplication (Supplementary Note 6).

At the core of the entire experiment lies a Markovian state-switching process based on the multistate $Sc_2C_2@C_{88}$ device. Experimentally, the Keithley 2450 source measure unit serves a dual purpose: it supplies a bias voltage to modulate the energy landscape of the cluster, thereby altering the state-transition matrix of the device, simultaneously reading the real-time current signal to determine the device state. Control and data processing are performed using LabVIEW and MATLAB (v.R2021b) routines, which periodically adjust the bias voltage of the device, acquire the latest conductance values, determine the corresponding state and accumulate the statistical results to perform matrix multiplication. In this way, each algorithmic step is directly conditioned on the intrinsic and unpredictable state transition of the cluster, effectively transforming the hardware itself into a high-precision matrix multiplier.

For device 2, we selected two voltages of 140 mV and 160 mV to demonstrate the matrix multiplication process described in Supplementary Note 6. With a time interval of 1 s, we recorded the initial and final states of the device under different voltage configurations, and each pair of initial and final states was recorded as one cycle. Figure 4a,d shows the state–cycle responses under biases of 140 mV and 160 mV, respectively, with four distinct conductance states marked in each plot. Figure 4b,e shows the state distribution histograms statistically obtained from the state–cycle relationships in Fig. 4a,d.

https://doi.org/10.1038/s41563-026-02609-3

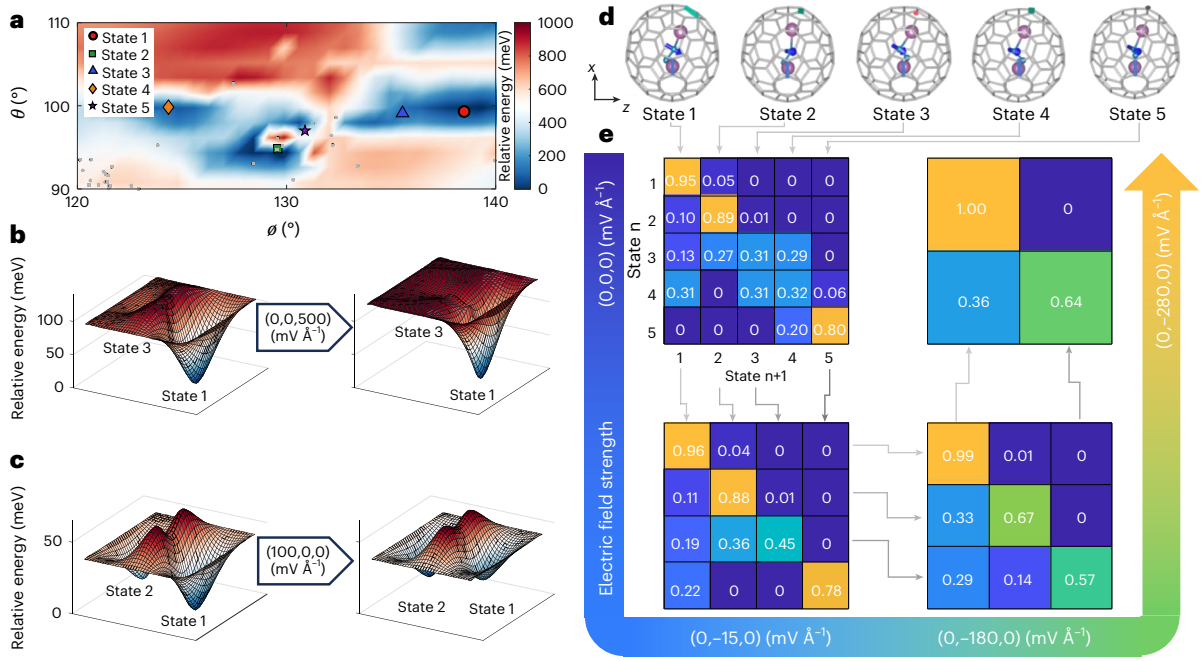

Fig. 5 | Evolution of rich energy landscapes driven by electric fields. a, PES of the $Sc_2C_2@C_{88}$ configurations. Different configurations are defined by the orientation of their Sc–Sc bond vector. Here ϕ and θ correspond to the angles between the Sc–Sc direction and the z and x axes, respectively. The red, green, blue, orange and purple points represent the five states with the highest values. All other computed configurations are indicated by black points. **b**,**c**, Electric field regulation of the PES: barrier modulation (**b**) and relative energy adjustment (**c**). **d**, Geometric configurations and electric dipole moment directions of the lowest-energy states. The blue arrows indicate the macroscopic electric dipole moment vectors. Different coloured markings on the surface of the carbon cage indicate the adsorption sites for Sc atoms. **e**, Evolution of the interstate-transition matrix under different external electric fields.

Figure 4c,f shows the state-transition matrices analysed from the data in Fig. 4a,d, using a time interval of 1 s and rounding of matrix elements to two decimal places. Furthermore, by repeatedly switching the voltage between 140 mV and 160 mV, we obtained the state–cycle response shown in Fig. 4g. The voltage was held for 1 s at each level; thus, the total duration of a single cycle was 2 s. Figure 4h shows the state distribution corresponding to the data in Fig. 4g. By statistically analysing the transition from the initial state to the final state within each cycle, we obtained the transition matrix shown in Fig. 4i. The matrix elements match the product of the matrices shown in Fig. 4c,f. Figure 4j presents a comparison between the measured matrix (yellow data) and the results obtained through direct calculation (blue data). The maximum and average errors among the matrix elements are less than 0.05 and 0.03 (Supplementary Fig. 20), respectively, thereby validating the high precision of matrix multiplication[41].

For comparison, memristor arrays are commonly used in matrix multiplication, in which the conductance weights of each device serve as the matrix elements. These conductance weights are applied to the input signals through Kirchhoff's laws, thereby naturally implementing matrix multiplication[21,42–45]. In $Sc_2C_2@C_{88}$ devices, matrix elements and multiplication can be realized in one device. In addition to the device structure mentioned in Fig. 1, we have designed and fabricated a four-nanowire array to further illustrate the small computing units and the potential of high integration density (Supplementary Figs. 9–12). We also demonstrated the probabilistic integer factorization and the state-transition-based matrix multiplication successfully (Supplementary Note 8).

Our current implementation relies on the intrinsic, fixed state-transition matrices of the device at specific bias voltages, which differs from the flexible, user-programmable matrix elements typical of memristor crossbar arrays. A future practical pathway could involve mapping a library of useful matrices (T_1, T_2…T_n) accessible under specific bias conditions. A user could then select and sequence these predefined matrices from the library to perform the desired computations, which establishes a novel paradigm for 'programming' computational operations in a single-cluster device by exploiting its rich physical tuning methods. To further unlock the potential of the matrix, we carried out a series of simulations. We could construct a Gaussian-type error production function capable of generating seven distinct error levels based on one 4 × 4 matrix, and simulate the neuromorphic diffusion process (Supplementary Note 9). Additionally, using the matrices as the weights, we successfully emulated colour recognition and classification (Supplementary Note 10). A training set consisting of 100 red, 100 green and 100 blue samples is used. The training error rapidly decreased to approximately ten misclassified samples within the first five epochs.

Discussion

Real-time in situ electrical measurements have been shown to be useful for probing latent electronic characteristics in devices[46]. The stochastic switching phenomenon is usually related to the evolution of the electronic states, which can be caused by evolution of the atomic structure when an electrical excitation is injected[27–29,47], geometrical fluctuations of the contact[48–50] or the influence of localized traps[51,52]. In our devices, the discrete states can remain stable for a long time according to the statistical histogram of the current distribution (Supplementary Note 5). These phenomena indicate that factors related to geometric fluctuations are unlikely. Besides, our transport data showed well-defined Coulomb diamond patterns (Fig. 1d) and differential conductance peaks, along with a bias window specific nature of the switching (Supplementary Note 2). All of these evidences are inconsistent with the behaviour of random external charge traps, further supporting an intrinsic origin. Therefore, we initially attributed the random switching between multiple distinct states to cluster structure evolution assisted by an electric field.

To elucidate the atomic configurations and their electric-field-driven switching mechanisms, we performed density functional theory (DFT) calculations on $Sc_2C_2@C_{88}$. By systematically considering

the C_{88} cage symmetry, Sc_2C_2 molecule orientation and C_2 dimer alignment, we generated 522 potential configurations (Methods). Figure 5a and Supplementary Fig. 29 present the mapped PES for the Sc_2C_2 orientation, revealing five distinct stable configurations (visualized in Fig. 5d and Supplementary Fig. 30) that are at least 30.4 meV more stable than other configurations, with the most stable structure being consistent with previous literature[17,53]. These states exhibit relative energy differences spanning 0.2–99.3 meV (Supplementary Table 2), indicating potential electric field tunability. All the configurations share a common structural feature: one Sc atom persistently occupies a C–C bridge site on the carbon cage. Differentiation between groups arises from distinct adsorption sites of the second Sc atom, whereas intragroup variations originate from rotational reorientations of the C_2 dimer.

We further performed climbing image nudged elastic band calculations to determine the transition pathways and energy barriers between all pairwise combinations of the five stable states (Supplementary Table 3). All five stable states and their transition states exhibit moderate electric dipole moments with distinct orientations (>0.39 e Å; Fig. 5d (blue arrows) and Supplementary Table 4). This substantial dipole variation enables dual electric field control mechanisms: (1) modulating relative state energies and (2) tuning interstate energy barriers. For example, a field of (0, 0, 500) mV $Å^{-1}$ field reduces the state 3 ↔ 1 barrier to zero and preserves the energy degeneracy between states 3 and 1 (Fig. 5b). A field of (100, 0, 0) mV $Å^{-1}$ inverts the stability hierarchy between states 2 and 1 and maintains a moderate barrier of 38 meV (Fig. 5c). Through Boltzmann statistics, we established a field-controllable probability matrix (calculation details are provided in the Methods). The applied electric field strength governs the effective sizes of the matrix (determined by the number of accessible states through selective barrier elimination) and the individual transition probabilities via continuous barrier height modulation. As shown in Fig. 5e, with increasing strength of the electric field along the *y* direction, the transition probability matrix undergoes simultaneous changes in the probability magnitudes and progressively reduces in size from 5 × 5 to 2 × 2. This allows us to access a set of different, precharacterized transition matrices from the same device, which also explains why stochastic switching in $Sc_2C_2@C_{88}$ devices is only prominent within a narrow bias window: at low voltages, the barrier-separating configurations cannot be surmounted, whereas at excessively high voltages, the energy landscape is so strongly distorted that the metastable wells vanish altogether. Therefore, the observed stochastic switching is fundamentally the electric-field-assisted rearrangement of the cluster configuration (Supplementary Videos 4 and 5) across its complex energy landscape.

Under this physical mechanism, the state of the device is determined solely by the current positions of the atoms, and any relaxation information from the past cannot be retained. This means that the state transitions of the device within a certain time interval depend only on its state in the previous time interval and are independent of earlier states. Therefore, we can analyse the results using a Markov model and compare them with the experimental results. We also measured the temperature dependence of stochastic switching (Supplementary Note 12). The results indicate that temperature does not significantly affect the time constant of the device. This finding suggests that the state transitions in the device are not dominantly caused by thermally activated processes induced by temperature but rather originate from the electric field (Supplementary Note 13).

Further, we fabricated devices with C_{88} deposited following the same procedure. Among all the tests, 15 devices exhibited Coulomb blockade (Supplementary Note 14). In these devices, the characteristic multilevel, voltage-controllable random switching observed in $Sc_2C_2@C_{88}$ was not detected. This further supports that the occurrence of random switching in our system can be primarily attributed to the presence of the encapsulated cluster inside the fullerene cage. Therefore, the intrinsic configurational dynamics of the $Sc_2C_2@C_{88}$ cluster, underpinned by its rich and electrically controllable energy landscape, can be harnessed to realize an ultra-compact, multilevel probabilistic unit. Considering the limitations of current fabrication techniques, more deterministic assembly methods would facilitate scalable high-temperature integration, advancing the translation of this material-level discovery into a viable technology for probabilistic and neuromorphic computing.

Conclusions

In summary, we investigated the multiple conductance states, probabilistic traversal and state-transition matrix in a $Sc_2C_2@C_{88}$ unit. The multiple conductance states switch randomly but controllably, and the confidence interval of the ACF of the random sequence is less than 0.02. On the basis of these characteristics, we demonstrated many potentialities of $Sc_2C_2@C_{88}$, including prime factorization and matrix multiplication. For matrix multiplication, the maximum error is small—less than 0.05. Combined with theoretical calculations, we uncovered the rich energy landscape in the ultra-compact unit, which paves the way for all-in-one ultra-compact intelligence.

Online content

Any methods, additional references, Nature Portfolio reporting summaries, source data, extended data, supplementary information, acknowledgements, peer review information; details of author contributions and competing interests; and statements of data and code availability are available at https://doi.org/10.1038/s41563-026-02609-3.

References

1. Markov, I. L. Limits on fundamental limits to computation. *Nature* **512**, 147–154 (2014).
2. Wang, H. et al. Scientific discovery in the age of artificial intelligence. *Nature* **620**, 47–60 (2023).
3. Adleman, L. M. Molecular computation of solutions to combinatorial problems. *Science* **266**, 1021–1024 (1994).
4. Cherry, K. M. & Qian, L. Scaling up molecular pattern recognition with DNA-based winner-take-all neural networks. *Nature* **559**, 370–376 (2018).
5. Woods, D. et al. Diverse and robust molecular algorithms using reprogrammable DNA self-assembly. *Nature* **567**, 366–372 (2019).
6. Lv, H. et al. DNA-based programmable gate arrays for general-purpose DNA computing. *Nature* **622**, 292–300 (2023).
7. Schirm, C. et al. A current-driven single-atom memory. *Nat. Nanotechnol.* **8**, 645–648 (2013).
8. Donati, F. et al. Magnetic remanence in single atoms. *Science* **352**, 318–321 (2016).
9. Kalff, F. E. et al. A kilobyte rewritable atomic memory. *Nat. Nanotechnol.* **11**, 926–929 (2016).
10. Natterer, F. D. et al. Reading and writing single-atom magnets. *Nature* **543**, 226–228 (2017).
11. Hus, S. M. et al. Observation of single-defect memristor in an MoS_2 atomic sheet. *Nat. Nanotechnol.* **16**, 58–62 (2021).
12. Vincent, R., Klyatskaya, S., Ruben, M., Wernsdorfer, W. & Balestro, F. Electronic read-out of a single nuclear spin using a molecular spin transistor. *Nature* **488**, 357–360 (2012).
13. Thiele, S. et al. Electrically driven nuclear spin resonance in single-molecule magnets. *Science* **344**, 1135–1138 (2014).
14. Goodwin, C. A. P., Ortu, F., Reta, D., Chilton, N. F. & Mills, D. P. Molecular magnetic hysteresis at 60 kelvin in dysprosocenium. *Nature* **548**, 439–442 (2017).
15. Kato, C. et al. Giant hysteretic single-molecule electric polarisation switching above room temperature. *Angew. Chem. Int. Ed.* **57**, 13429–13432 (2018).
16. Zhang, K. et al. A $Gd@C_{82}$ single-molecule electret. *Nat. Nanotechnol.* **15**, 1019–1024 (2020).

17. Li, J. et al. Room-temperature logic-in-memory operations in single-metallofullerene devices. *Nat. Mater.* **21**, 917–923 (2022).
18. Athmanathan, A., Stanisavljevic, M., Papandreou, N., Pozidis, H. & Eleftheriou, E. Multilevel-cell phase-change memory: a viable technology. *IEEE J. Emerg. Sel. Topics Circuits Syst.* **6**, 87–100 (2016).
19. Goswami, S. et al. Decision trees within a molecular memristor. *Nature* **597**, 51–56 (2021).
20. Rao, M. et al. Thousands of conductance levels in memristors integrated on CMOS. *Nature* **615**, 823–829 (2023).
21. Sharma, D. et al. Linear symmetric self-selecting 14-bit kinetic molecular memristors. *Nature* **633**, 560–566 (2024).
22. Correll, J. M. et al. An 8-bit 20.7 TOPS/W multilevel cell ReRAM macro with ADC-assisted bit-serial processing. *IEEE J. Solid-State Circuits* **60**, 2995–3008 (2025).
23. Borders, W. A. et al. Integer factorization using stochastic magnetic tunnel junctions. *Nature* **573**, 390–393 (2019).
24. Roques-Carmes, C. et al. Biasing the quantum vacuum to control macroscopic probability distributions. *Science* **381**, 205–209 (2023).
25. Wang, K. et al. Single skyrmion true random number generator using local dynamics and interaction between skyrmions. *Nat. Commun.* **13**, 722 (2022).
26. Wang, Y. et al. Superior probabilistic computing using operationally stable probabilistic-bit constructed by a manganite nanowire. *Natl Sci. Rev.* **12**, nwae338 (2025).
27. Chandler, H. J., Stefanou, M., Campbell, E. E. B. & Schaub, R. Li@C_{60} as a multi-state molecular switch. *Nat. Commun.* **10**, 2283 (2019).
28. Huang, T. et al. A molecular switch based on current-driven rotation of an encapsulated cluster within a fullerene cage. *Nano Lett.* **11**, 5327–5332 (2011).
29. Auwärter, W. et al. A surface-anchored molecular four-level conductance switch based on single proton transfer. *Nat. Nanotechnol.* **7**, 41–46 (2012).
30. Wang, F. et al. Electrically controlled nonvolatile switching of single-atom magnetism in a Dy@C_{84} single-molecule transistor. *Nat. Commun.* **15**, 2450 (2024).
31. Yuan, X. H. et al. Arbitrary modulation of average dwell time in discrete-time Markov chains based on tunneling magnetoresistance effect. *IEEE Electron Device Lett.* **45**, 1349–1352 (2024).
32. Larimian, S., Mahmoodi, M. R. & Strukov, D. B. Lightweight integrated design of PUF and TRNG security primitives based on eFlash memory in 55-nm CMOS. *IEEE Trans. Electron Devices* **67**, 1586–1592 (2020).
33. Ding, Q. et al. Unified 0.75 pJ/bit TRNG and attack resilient $2F^2$/bit PUF for robust hardware security solutions with 4-layer stacking 3D NbO_x threshold switching array. *IEDM* **39**, 1–4 (2021).
34. Shen, B. et al. Harnessing microcomb-based parallel chaos for random number generation and optical decision making. *Nat. Commun.* **14**, 4590 (2023).
35. Ravichandran, H. et al. A stochastic encoder using point defects in two-dimensional materials. *Nat. Commun.* **15**, 10562 (2024).
36. Preston, R. J., Kershaw, V. F. & Kosov, D. S. Current-induced atomic motion, structural instabilities, and negative temperatures on molecule-electrode interfaces in electronic junctions. *Phys. Rev. B* **101**, 155415 (2020).
37. Rudge, S. L. & Kosov, D. S. Distribution of waiting times between electron cotunneling events. *Phys. Rev. B* **98**, 245402 (2018).
38. Rudge, S. L. & Kosov, D. S. Fluctuating-time and full counting statistics for quantum transport in a system with internal telegraphic noise. *Phys. Rev. B* **100**, 235430 (2019).
39. Niazi, S. et al. Training deep Boltzmann networks with sparse Ising machines. *Nat. Electron.* **7**, 610–619 (2024).
40. Tian, H. et al. A hardware Markov chain algorithm realized in a single device for machine learning. *Nat. Commun.* **9**, 4305 (2018).
41. Sun, Z. et al. Solving matrix equations in one step with cross-point resistive arrays. *Proc. Natl Acad. Sci. USA* **116**, 4123–4128 (2019).
42. Duan, X. G. et al. Memristor-based neuromorphic chips. *Adv. Mater.* **36**, 2310704 (2024).
43. Cai, F. X. et al. A fully integrated reprogrammable memristor-CMOS system for efficient multiply-accumulate operations. *Nat. Electron.* **2**, 290–299 (2019).
44. Jeong, H. et al. Self-supervised video processing with self-calibration on an analogue computing platform based on a selector-less memristor array. *Nat. Electron.* **8**, 168–178 (2025).
45. Zhang, W. B. et al. Edge learning using a fully integrated neuro-inspired memristor chip. *Science* **381**, 1205–1211 (2023).
46. Kim, Y. & Song, H. Noise spectroscopy of molecular electronic junctions. *Appl. Phys. Rev.* **8**, 011303 (2021).
47. Guo, Y. et al. Emergent complexity of quantum rotation tunneling. *Sci. Adv.* **11**, eads0503 (2025).
48. Dulić, D. et al. Controlled stability of molecular junctions. *Angew. Chem. Int. Ed.* **48**, 8273–8276 (2009).
49. Kihira, Y., Shimada, T., Matsuo, Y., Nakamura, E. & Hasegawa, T. Random telegraphic conductance fluctuation at Au–pentacene–Au nanojunctions. *Nano Lett.* **9**, 1442–1446 (2009).
50. Park, Y. et al. Atomic-precision control of plasmon-induced single-molecule switching in a metal–semiconductor nanojunction. *Nat. Commun.* **15**, 6709 (2024).
51. Kim, Y., Song, H., Kim, D., Lee, T. & Jeong, H. Noise characteristics of charge tunneling via localized states in metal–molecule–metal junctions. *ACS Nano* **4**, 4426–4430 (2010).
52. Arielly, R., Vadai, M., Kardash, D., Noy, G. & Selzer, Y. Real-time detection of redox events in molecular junctions. *J. Am. Chem. Soc.* **136**, 2674–2680 (2014).
53. Chen, C.-H. et al. Zigzag Sc_2C_2 carbide cluster inside a [88] fullerene cage with one heptagon, Sc_2C_2@Cs(hept)-C_{88}: a kinetically trapped fullerene formed by C_2 insertion? *J. Am. Chem. Soc.* **138**, 13030–13037 (2016).

[1]National Laboratory of Solid State Microstructures, Collaborative Innovation Center of Advanced Microstructures, School of Physics, Nanjing University, Nanjing, China. [2]Institute of Atomic Scale Manufacturing, Nanjing University, Nanjing, China. [3]Nanjing Institute of Atomic Scale Manufacturing, Nanjing, China. [4]Beijing Key Laboratory of Optoelectronic Functional Materials and Micro-Nano School of Physics, Renmin University of China, Beijing, China. [5]State Key Laboratory of Physical Chemistry of Solid Surfaces, College of Chemistry and Chemical Engineering, Xiamen University, Xiamen, China. [6]National Key Laboratory for Novel Software Technology, School of Artificial Intelligence, Nanjing University, Nanjing, China. [7]Key Laboratory of Quantum Theory and Applications of MoE, Lanzhou Center for Theoretical Physics, and Key Laboratory of Theoretical Physics of Gansu Province, Lanzhou University, Lanzhou, China. [8]State Key Laboratory of Spintronics, School of Electronic Science and Engineering, Collaborative Innovation Center of Advanced Microstructures, Nanjing University, Nanjing, China. [9]These authors contributed equally: Haoran Qi, Guohao Xi, Yuan-Biao Zhou, Xinrong Liu, Yifu Mao. ✉e-mail: zhangminhao@nju.edu.cn; wcphys@ruc.edu.cn; yuanzhi_tan@xmu.edu.cn; songfengqi@nju.edu.cn

Methods

Fabrication of $Sc_2C_2@C_{88}$ cluster device

Supplementary Note 1 provides details, including substrate preparation and electrode/nanowire patterning, synthesis and characterization of the $Sc_2C_2@C_{88}$ cluster, formation of a single-cluster junction via feedback-controlled electromigration and so on. It is crucial to clarify here that the nanowire, which forms the core of the device, is patterned using electron-beam lithography. This nanowire has a nominal minimum width of 50 nm and a length of approximately 400 nm.

Experimental setup

All the transport measurements were performed in a cryogen-free high-magnetic-field cryogenic system (Cryogenic Limited) with a base temperature of 1.8 K to ensure electrode stability. The device was wire bonded to a sample stage, and all electrical connections were made via cryogenic wiring to the room-temperature instrumentation. The Keithley 2450 source meters provided the necessary microvolt precision and current sensitivity for single-cluster transport measurements. The entire measurement sequence—including voltage output, data acquisition and real-time control logic—was orchestrated by the LabVIEW program via GPIB communication. Therefore, there is a direct and causal connection between the measured stochastic properties of the $Sc_2C_2@C_{88}$ device and the computing results presented.

Factorization algorithm

Using the Keithley 2450 device as a digital-to-analogue converter, we applied inputs to the device and directed the outputs through a circuit board into a computer. The entire process was controlled by a LabVIEW program, which implemented an algorithm to minimize the cost function E. In the experiment, the initial probability of the p-bit was set to 0.5. We saved the voltage that was to be input into the device in the form of an array, sequentially applied it to the p-bit units, and recorded the output of the p-bit units in an array one by one. We assigned the output results to the corresponding bit positions of the two factors and carried out further calculations. The ith bit position could be driven by voltage input V_i. The adjustment value for V_i after each learning iteration was calculated as follows:

$$\Delta V_i = -\partial E/\partial m_i,$$

where m_i is the output of the ith bit position, expressed in binary form.

Starting from the form of the cost function E, we assumed that the number F to be factored could be expressed as the product of two odd numbers X and Y, both greater than or equal to 3 (because even numbers can be quickly preprocessed and the factor of 1 is trivial). This was achieved via the following relations:

$$E = (XY - F)^2,$$

$$X = 3 + \sum_{i=1}^{n} 2^{i-1} m_i,$$

$$Y = 3 + \sum_{j=1}^{n} 2^{j-1} m_j.$$

Throughout the learning process, we imposed probability constraints, requiring the probability range of the p-bit to be [0.1, 0.9]. This ensured that even when the device entered a local minimum, it could still escape after a few learning iterations. When the learning process resulted in $E = 0$, the loop was exited, and the result was output.

Theoretical calculations

Our DFT calculations were performed using the generalized gradient approximation and the projector augmented-wave method[54,55] as implemented in the Vienna ab initio simulation package[56]. The Perdew–Burke–Ernzerhof function[57] with D3 dispersion correction[58] was used. The kinetic energy cut-off was set to 400 eV. A $25 \times 25 \times 25$ Å^3 supercell was used to model the isolated $Sc_2C_2@C_{88}$ molecule, which ensured a separation of at least 17 Å between the molecule and its images (Supplementary Fig. 31). The Γ point was used for sampling the first Brillouin zone in all calculations. All the atoms were allowed to relax until the residual force on each atom was less than 0.01 eV Å^{-1}.

Transition pathways and energy barriers were revealed by the climbing image nudged elastic band method[59,60], which locates the exact saddle point of a reaction pathway. The electric dipole moments of the C_{88} molecule system were calculated on the basis of the classical definition:

$$P = \frac{1}{V}\left(-e\sum_j Z_j u_j\right) + \int r\rho(r)\mathrm{d}r,$$

where e is the electron charge; V is the cell volume; Z_j and u_j are the atomic number and position of atom j, respectively; and ρ(r) is the electronic charge density at location r in real space. Dipole correction was considered in all calculations to correct the error introduced by the periodic boundary condition and balance the vacuum-level differences on the different sides of the polarized molecules[61,62].

The interstate-transition probability model based on the Boltzmann distribution[63,64] can be expressed as follows: for any given microscopic state i in the system, the transition probability to a target state j is given by

$$P_{i\to j} = \frac{\mathrm{e}^{-\Delta E_{ij}/(k_\mathrm{B}T)}}{Z_i},$$

$$Z_i = \sum \mathrm{e}^{-\frac{\Delta E_{ij}}{k_\mathrm{B}T}},$$

where ΔE_{ij} represents the energy barrier per atom to overcome for the transition from state i to state j, k_B is the Boltzmann constant, T is the thermodynamic temperature (2 K) of the system and Z_i is the partition function for probability normalization.

Screening of stable configurations of $Sc_2C_2@C_{88}$

We considered inequivalent adsorption sites for the two Sc atoms of the Sc_2C_2 molecule inside the C_s(hept)-C_{88} cage, including hollow sites above the $C_5/C_6/C_7$ rings, C–C bonds and top sites above the C atoms (totalling 145 types of site). On the basis of the Sc–C bond length (~2.1 Å) and C–C bond length (~1.2 Å) within the Sc_2C_2 molecule, along with the orientation of C_2, we constrained the Sc–Sc distance to 3.6–4.7 Å and applied mirror symmetry, ultimately identifying 370 candidate configurations. After identifying the relatively stable Sc_2C_2 adsorption configurations, we further considered the spatial orientation of the central C_2 dimer bridge within the Sc_2C_2 molecule for the five most stable configurations, which led to the calculation of an additional 152 configurations. Following structural optimization and total energy comparison via first-principles calculations, we discarded configurations with significantly higher energies or those unable to maintain structural stability. This screening yielded the five stable configurations mentioned in the main text (Fig. 5). On the basis of the calculated energies of these structures, we constructed a PES for $Sc_2C_2@C_{88}$ (Fig. 5a and Supplementary Fig. 29). Linear interpolation was used to depict the energies between the points on the PES corresponding to the calculated configurations.

Data availability

The data supporting the findings of this study are available within this Article and its Supplementary Information. Source data are provided with this paper. Additional data are available from the corresponding authors upon request.

References

54. Blöchl, P. E. Projector augmented-wave method. *Phys. Rev. B* **50**, 17953–17979 (1994).
55. Kresse, G. & Joubert, D. From ultrasoft pseudopotentials to the projector augmented-wave method. *Phys. Rev. B* **59**, 1758–1775 (1999).
56. Kresse, G. & Furthmüller, J. Efficient iterative schemes for ab initio total-energy calculations using a plane-wave basis set. *Phys. Rev. B* **54**, 11169–11186 (1996).
57. Perdew, J. P., Burke, K. & Ernzerhof, M. Generalized gradient approximation made simple. *Phys. Rev. Lett.* **77**, 3865–3868 (1996).
58. Grimme, S., Antony, J., Ehrlich, S. & Krieg, H. A consistent and accurate ab initio parametrization of density functional dispersion correction (DFT-D) for the 94 elements H-Pu. *J. Chem. Phys.* **132**, 154104 (2010).
59. Hong, J. et al. Exploring atomic defects in molybdenum disulphide monolayers. *Nat. Commun.* **6**, 6293 (2015).
60. Qiao, J., Kong, X., Hu, Z.-X., Yang, F. & Ji, W. High-mobility transport anisotropy and linear dichroism in few-layer black phosphorus. *Nat. Commun.* **5**, 4475 (2014).
61. Qiao, J. et al. Few-layer tellurium: one-dimensional-like layered elementary semiconductor with striking physical properties. *Sci. Bull.* **63**, 159–168 (2018).
62. Zhao, Y. et al. Extraordinarily strong interlayer interaction in 2D layered PtS_2. *Adv. Mater.* **28**, 2399–2407 (2016).
63. Boltzmann, L. Studies on the balance of living force between moving material points. *Wiener Ber.* **58**, 517–560 (1868).
64. Zierenberg, J., Schierz, P. & Janke, W. Canonical free-energy barrier of particle and polymer cluster formation. *Nat. Commun.* **8**, 14546 (2017).

Acknowledgements

F.S. acknowledges the National Natural Science Foundation of China (grant numbers 92161201, 12025404 and T2221003), the National Key R&D Program of China (grant number 2022YFA1402404), the Fundamental and Interdisciplinary Disciplines Breakthrough Plan of the Ministry of Education of China (grant number JYB2025XDXM411) and the Natural Science Foundation of Jiangsu Province (grant numbers BK20243013 and BK20233001). M.Z. acknowledges the National Natural Science Foundation of China (grant numbers 92577205 and 12422410). C.W. acknowledges the Young Elite Scientists Sponsorship Program of the Beijing High Innovation Plan (number 20250666), the Fundamental Research Funds for the Central Universities and the Research Funds of Renmin University of China (grant number 24XNKJ17). All calculations for this study were performed at the Physics Lab of High-Performance Computing (PLHPC) and the Public Computing Cloud (PCC) of Renmin University of China. K.H. acknowledges the National Natural Science Foundation of China (grant number 12474272). S.Z. acknowledges the National Natural Science Foundation of China (grant numbers 92580203 and 12374043) and the Natural Science Foundation of Jiangsu Province (grant number BK20240166). X.W. acknowledges the National Natural Science Foundation of China (grant numbers 62525406, T2394473 and 62274085). W.J. acknowledges the National Natural Science Foundation of China (grant numbers 92477205 and 52461160327) and the National Key R&D Program of China (grant number 2023YFA1406500).

Author contributions

M.Z., Y.-Z.T. and F.S. conceived the idea for the paper. Y.-B.Z., Y.-Z.T. and S.-Y.X. synthesized and characterized the endohedral metallofullerene. H.Q., X.L., Y.M., J.Y. and J.C. fabricated the transistors. H.Q., X.L. and Y.M. constructed the measurements. H.Q. designed the circuit. G.X., C.W. and W.J. conducted the theoretical calculations. H.Q., G.X., Y.-B.Z., X.L., K.H., W.G., S.Z., X.G., J.W., D.-W.Z., J.A., X.W., D.-C.Z., M.Z., C.W., W.J., Y.-Z.T., S.-Y.X. and F.S. analysed and discussed the data and wrote the paper. F.S. and Y.-Z.T. supervised the project.

Competing interests

The authors declare no competing interests.

Additional information

Supplementary information The online version contains supplementary material available at https://doi.org/10.1038/s41563-026-02609-3.

Correspondence and requests for materials should be addressed to Minhao Zhang, Cong Wang, Yuan-Zhi Tan or Fengqi Song.

Peer review information *Nature Materials* thanks Mario Lanza and the other, anonymous, reviewer(s) for their contribution to the peer review of this work.